

ABSTRACT: A finite element model of localized deformation in frictional materials taking a strong discontinuity approach is presented. A non-associated Drucker-Prager plasticity model is formulated in the context of strong discontinuities and implemented within the framework of the assumed enhanced strain finite element method. The model is used to simulate the load-displacement behavior of soft rock under plane strain loading, approximately capturing the failure surface orientation and the subsequent softening portion of the load-displacement curve without demonstrating mesh dependence.

1 INTRODUCTION

Localized deformation in the form of shear bands and slip surfaces occurs naturally in frictional materials like soil and rock as a result of material inhomogeneities. Such deformation is typically followed by a reduction in overall strength of the material body as loading proceeds. Much experimental work has been conducted to understand the inception of localized deformation in soil and rock by relating the microscopic behavior (e.g. micro-cracking in brittle rock, mineral particle rolling and sliding in granular soil, and mineral particle rotation and translation in the cement matrix of soft rock like sandstone) to the macroscopic behavior via overall load-displacement curves (Vardoulakis & Goldschieder 1981, Santarelli & Brown 1989, Wawersik et al. 1990, Ord et al. 1991, and Labuz et al. 1996, to name a few). This paper attempts to numerically model localized deformation from the macroscopic standpoint by matching experimental load-displacement curves to finite element solutions without exhibiting mesh dependence. There have been many attempts to numerically model localized deformation and the subsequent softening region of the load-displacement curve from the continuum perspective while avoiding mesh dependence (called “regularizing” the problem): length-scale incorporated in the plastic evolution equations (Pietruszczak & Mróz 1981),

non-local approach (Bažant & Pijaudier-Cabot 1988, Adachi et al. 1991), adaptive remeshing (Zienkiewicz et al. 1995), weak discontinuity approach (Ortiz et al. 1987), element breaking (Wan et al. 1990), and the strong discontinuity approach (Simo et al. 1993, Simo & Oliver 1994, Larson & Runesson 1993, Armero & Garikipati 1995, 1996), to name a few. There has also been an effort to bring together many of these methods under the umbrella of a general, multiscale finite element method (Garikipati & Hughes 1998).

This paper takes the strong discontinuity approach developed by Simo and co-workers to model localized deformation in frictional materials because a finite element model based on this approach produces mesh-independent solutions—objective with respect to mesh refinement and insensitive to mesh alignment—without introducing ad hoc treatments like a characteristic length scale. The remainder of this paper presents the formulation of a pressure-dependent, non-associated plasticity model (in this case, Drucker-Prager) in the context of strong discontinuities and its implementation within the framework of the assumed enhanced strain finite element method. A numerical example demonstrates the ability of the model to approximate—in a mesh-independent manner—the localized deformation pattern and load-displacement curve resulting from a plane strain compression experiment on a Gosford sand-

stone. Note that it would be incorrect to use failure parameters determined from triaxial compression tests in a plane strain finite element simulation (see experimental comparisons by Yumlu & Ozbay 1995) and that it would be incorrect to use an axisymmetric stress condition to model strain localization in a triaxial compression specimen (see Fig. 8 of Adachi et al. 1991, which represents a barreling deformation pattern as opposed to the formation of a failure surface). Continuum mechanics convention is followed throughout the paper. Formulations are carried out in the infinitesimal strain regime.

2 KINEMATICS OF STRONG DISCONTINUITY

In the context of this paper, a strong discontinuity refers to a jump in displacement, as opposed to a weak discontinuity which denotes a jump in strain (see Kachanov 1971). It has been proven that such displacement jumps are admissible solutions to the perfectly-plastic infinitesimal plasticity problem and that the appropriate space of admissible solutions is called the “bounded deformation space” (Matthies et al. 1979). Consider the following decomposition of the displacement rate vector:

$$\dot{\mathbf{u}} = \dot{\hat{\mathbf{u}}} + [[\dot{\mathbf{u}}]] H_S(\mathbf{x}) \quad (1)$$

$$H_S(\mathbf{x}) = \begin{cases} 1 & \text{if } \mathbf{x} \in \Omega_+ \\ 0 & \text{if } \mathbf{x} \in \Omega_- \end{cases} \quad (2)$$

where $\dot{\hat{\mathbf{u}}}$ is the continuous part of $\dot{\mathbf{u}}$, $[[\dot{\mathbf{u}}]] = \dot{\mathbf{u}}_+ - \dot{\mathbf{u}}_-$ is the jump displacement rate across the discontinuity \mathcal{S} (see Fig. 1), and $H_S(\mathbf{x})$ is the Heaviside function at \mathcal{S} .

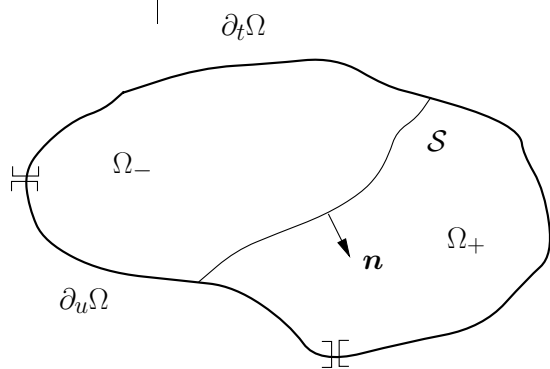


Figure 1. Body $\bar{\Omega}$ with discontinuity \mathcal{S} ($\Omega = \Omega_+ \cup \Omega_-$, $\partial\Omega = \partial_t\Omega \cup \partial_u\Omega \cup \mathcal{S}$, $\bar{\Omega} = \Omega \cup \partial\Omega$).

Using a standard result from the theory of distributions (Stakgold 1979), the small strain rate tensor is defined as (Simo et al. 1993)

$$\dot{\epsilon} := \nabla^s \dot{\mathbf{u}} = \nabla^s \dot{\hat{\mathbf{u}}} + ([[\dot{\mathbf{u}}]] \otimes \mathbf{n})^s \delta_{\mathcal{S}} \quad (3)$$

where $(\cdot)^s$ denotes the symmetric part, \mathbf{n} is the unit normal to the discontinuity surface \mathcal{S} pointing into Ω_+ , and $\delta_{\mathcal{S}}$ is the Dirac-delta function on the discontinuity surface \mathcal{S} . The displacement jump rate is defined as $[[\dot{\mathbf{u}}]] = \dot{\zeta} \mathbf{m}$, where $\dot{\zeta}$ is the magnitude of $[[\dot{\mathbf{u}}]]$ and \mathbf{m} is the direction.

A jump in displacement (resulting in infinite strain at \mathcal{S}) is an adequate approximation to the actual localized deformation pattern observed in soft rock, as shown experimentally (Ord et al. 1991, Labuz et al. 1996).

3 NON-ASSOCIATED DRUCKER-PRAGER PLASTICITY WITH STRONG DISCONTINUITY

A non-associated plasticity model is formulated within the context of strong discontinuities and is specialized for Drucker-Prager plasticity (see Borja & Regueiro 1998 for details).

3.1 Non-associated plasticity

Given a free energy function $\Psi(\epsilon^e, \xi)$ defined in terms of the elastic strain tensor ϵ^e and the strain-like vector of plastic internal variables ξ , the Cauchy stress σ and stress-like vector of plastic internal variables α are defined as

$$\sigma = \frac{\partial \Psi(\epsilon^e, \xi)}{\partial \epsilon^e}, \quad \alpha = -\frac{\partial \Psi(\epsilon^e, \xi)}{\partial \xi}. \quad (4)$$

Given a yield function $\phi(\sigma, \alpha)$ and plastic potential function $\varphi(\sigma, \alpha)$, the evolution equations are

$$\dot{\epsilon}^e = \dot{\epsilon} - \lambda \frac{\partial \varphi(\sigma, \alpha)}{\partial \sigma}, \quad \dot{\xi} = \lambda \frac{\partial \varphi(\sigma, \alpha)}{\partial \alpha} \quad (5)$$

where $\dot{\epsilon}^p = \lambda \partial \sigma \varphi$ is the plastic strain rate and λ is the plastic consistency parameter. Associated plasticity is attained by $\partial \sigma \varphi = \partial \sigma \phi$, and associated hardening by $\partial \alpha \varphi = \partial \alpha \phi$. The classical Kuhn-Tucker complementary conditions for loading and unloading hold

$$\lambda \geq 0, \quad \phi(\sigma, \alpha) \leq 0, \quad \lambda \phi(\sigma, \alpha) = 0 \quad (6)$$

as well as the consistency condition

$$\lambda \dot{\phi}(\boldsymbol{\sigma}, \boldsymbol{\alpha}) = 0. \quad (7)$$

In the next section, the non-associated plasticity model is formulated in the context of strong discontinuities.

3.2 Non-associated plasticity with strong discontinuity

It is assumed that for a plasticity model with strong discontinuity, plastic flow is localized to the discontinuity, and thus the plastic consistency parameter becomes a singular distribution

$$\lambda = \lambda_\delta \delta_{\mathcal{S}}. \quad (8)$$

Because the consistency condition must be satisfied pointwise, it is seen that the inverse of the hardening/softening moduli matrix must also be a singular distribution

$$\mathbf{H}^{-1} = \mathbf{H}_\delta^{-1} \delta_{\mathcal{S}}. \quad (9)$$

Equation (9) implies that softening is localized to the discontinuity. Equilibrium requires that the traction be continuous across \mathcal{S} (i.e. a regular distribution), and thus its singular part must vanish

$$\dot{\mathbf{t}}_\delta = \mathbf{0}. \quad (10)$$

Equation (10) leads to the localization condition

$$\mathbf{A} \cdot \mathbf{m} = \mathbf{0}, \quad \mathbf{A} = \mathbf{n} \cdot \mathbf{C}^{ep} \cdot \mathbf{n} \quad (11)$$

where \mathbf{A} is the elastic perfectly-plastic acoustic tensor, and \mathbf{C}^{ep} is the elastic perfectly-plastic tangent modulus tensor

$$\mathbf{C}^{ep} = \mathbf{C} - \frac{\mathbf{C} : \partial_{\boldsymbol{\sigma}} \phi \otimes \partial_{\boldsymbol{\sigma}} \phi : \mathbf{C}}{\partial_{\boldsymbol{\sigma}} \phi : \mathbf{C} : \partial_{\boldsymbol{\sigma}} \phi} \quad (12)$$

where $\mathbf{C} = \partial_{\boldsymbol{\epsilon}^e \boldsymbol{\epsilon}^e}^2 \Psi(\boldsymbol{\epsilon}^e, \boldsymbol{\xi})$. Thus, Eq. (11) implies that for $\mathbf{m} \neq \mathbf{0}$, $(\mathbf{m} \otimes \mathbf{n})^s$ must lie in the nullspace of \mathbf{C}^{ep} for loss of strong ellipticity of \mathbf{A} to occur (see Hill 1962 and Rice 1976 for discussions of loss of strong ellipticity). By satisfaction of the consistency condition, the stress-displacement relation along the discontinuity takes the form

$$\dot{\zeta} = \frac{\text{tr}(\partial_{\boldsymbol{\sigma}} \phi)}{\mathcal{H}_\delta \mathbf{m} \cdot \mathbf{n}} \frac{\partial \phi}{\partial \boldsymbol{\sigma}} : \dot{\boldsymbol{\sigma}} \quad (13)$$

where $\mathcal{H}_\delta = \partial_{\boldsymbol{\alpha}} \phi \cdot \mathbf{H}_\delta \cdot \partial_{\boldsymbol{\alpha}} \phi$ and $\text{tr}(\cdot)$ denotes the trace of a second order tensor.

A calculation of the dissipation produced by a plasticity model with strong discontinuity demonstrates an important attribute of the strong discontinuity approach. The dissipation function is defined as (Lublner 1990, Simo 1996)

$$\mathcal{D} = \boldsymbol{\sigma} : \dot{\boldsymbol{\epsilon}} - \dot{\Psi}(\boldsymbol{\epsilon}^e, \boldsymbol{\xi}) \quad (14)$$

where $\boldsymbol{\sigma} : \dot{\boldsymbol{\epsilon}}$ is the stress power and, for quasi-static formulations, the total external power input into the system, while $\dot{\Psi}$ represents the power existing within the body. The free energy rate is

$$\dot{\Psi}(\boldsymbol{\epsilon}^e, \boldsymbol{\xi}) = \boldsymbol{\sigma} : \dot{\boldsymbol{\epsilon}} - \lambda(\boldsymbol{\sigma} : \partial_{\boldsymbol{\sigma}} \phi + \boldsymbol{\alpha} \cdot \partial_{\boldsymbol{\alpha}} \phi) \quad (15)$$

and thus

$$\mathcal{D} = \lambda(\boldsymbol{\sigma} : \partial_{\boldsymbol{\sigma}} \phi + \boldsymbol{\alpha} \cdot \partial_{\boldsymbol{\alpha}} \phi) = \mathcal{D}_\delta \delta_{\mathcal{S}}. \quad (16)$$

Integrating Eq. (16) over a region Ω , it is seen that the total rate of dissipation \mathcal{D}_Ω is calculated over a set of zero measure, in this case the discontinuity surface \mathcal{S} :

$$\mathcal{D}_\Omega = \int_{\mathcal{S}} \lambda_\delta (\boldsymbol{\sigma} : \partial_{\boldsymbol{\sigma}} \phi + \boldsymbol{\alpha} \cdot \partial_{\boldsymbol{\alpha}} \phi) d\mathcal{S}. \quad (17)$$

This calculation of total dissipation reveals that a finite element model drawing its constitutive behavior from a plasticity model with strong discontinuity will be objective with respect to mesh refinement.

3.3 Specialize for Drucker-Prager plasticity

Using the framework developed in the previous two sections, a non-associated Drucker-Prager plasticity model is presented in order to be able to model pressure-dependent, frictional materials like soil and rock. Given a quadratic free energy function

$$\Psi(\boldsymbol{\epsilon}^e, \boldsymbol{\xi}) = \frac{1}{2} \boldsymbol{\epsilon}^e : \mathbf{c}^e : \boldsymbol{\epsilon}^e + \frac{1}{2} \boldsymbol{\xi} \cdot \mathbf{H} \cdot \boldsymbol{\xi} \quad (18)$$

linear elasticity and linear hardening result:

$$\boldsymbol{\sigma} = \mathbf{c}^e : \boldsymbol{\epsilon}^e, \quad \boldsymbol{\alpha} = -\mathbf{H} \cdot \boldsymbol{\xi}. \quad (19)$$

The elastic tangent modulus tensor is defined as

$$\mathbf{c}^e = K \mathbf{1} \otimes \mathbf{1} + 2\mu (\mathbf{I} - \frac{1}{3} \mathbf{1} \otimes \mathbf{1}) \quad (20)$$

where K and μ are the elastic bulk and shear moduli, respectively, and \mathbf{I} is the fourth order identity tensor. The hardening/softening moduli matrix and the strain-like vector of plastic internal variables are defined as

$$\mathbf{H} = \begin{bmatrix} K' & 0 \\ 0 & H' \end{bmatrix}, \quad \boldsymbol{\xi} = \begin{Bmatrix} v^p \\ e^p \end{Bmatrix} \quad (21)$$

where K' and H' are the standard volumetric and shear hardening/softening moduli, $v^p = \text{tr}(\dot{\boldsymbol{\epsilon}}^p)$, $e^p = \sqrt{\frac{2}{3}} \|\dot{\boldsymbol{\epsilon}}^p\|$, and $\dot{\boldsymbol{\epsilon}}^p = \dot{\boldsymbol{\epsilon}}^p - (v^p/3)\mathbf{1}$; \mathbf{H}_δ , K_δ , and

H_δ are defined similarly for the post-localization problem.

The yield function ϕ and plastic potential function φ are defined as

$$\begin{aligned}\phi(\boldsymbol{\sigma}, \boldsymbol{\alpha}) &= \sqrt{\frac{3}{2}}\|\mathbf{s}\| + \sqrt{3}(\alpha + \beta p) = 0 \\ \varphi(\boldsymbol{\sigma}, \boldsymbol{\alpha}) &= \sqrt{\frac{3}{2}}\|\mathbf{s}\| + \sqrt{3}(\alpha + bp) \\ \alpha &:= -\alpha_0 + b\alpha_1 + \alpha_2/\sqrt{3}\end{aligned}\quad (22)$$

where $\mathbf{s} = \boldsymbol{\sigma} - p\mathbf{1}$ is the deviatoric stress, $p = \frac{1}{3}\text{tr}(\boldsymbol{\sigma})$, α_1 and α_2 are the volumetric and shear components, respectively, of $\boldsymbol{\alpha}$, α_0 and β are defined in terms of the cohesion \bar{c} and friction angle $\bar{\phi}$ as (Owen & Hinton 1980)

$$\begin{aligned}\alpha_0 &= \frac{6\bar{c}\cos\bar{\phi}}{\sqrt{3}(3 + A\sin\bar{\phi})}, \\ \beta &= \frac{6\sin\bar{\phi}}{\sqrt{3}(3 + A\sin\bar{\phi})}, \\ -1 &\leq A \leq 1.\end{aligned}\quad (23)$$

The value $A = -1$ coincides with a cone that circumscribes the Mohr-Coulomb envelope, and $A = 1$ coincides with a cone which inscribes the Mohr-Coulomb envelope. The material dilation constant b is defined similarly as β in terms of the dilation angle $\bar{\psi}$ as

$$b = \frac{6\sin\bar{\psi}}{\sqrt{3}(3 + A\sin\bar{\psi})}.\quad (24)$$

Notice that we have associated plasticity if $\bar{\phi} = \bar{\psi}$, but typically for soil and rock this is not the case. Usually, $\bar{\phi} > \bar{\psi}$ with $\bar{\psi} > 0$ for a dilatant material and $\bar{\psi} < 0$ for a contractant material.

For the plane strain stress condition, the localization condition $\mathbf{A} \cdot \mathbf{m} = \mathbf{0}$ reduces to

$$\frac{\|\mathbf{s}\|}{\sqrt{2}r} = \sqrt{\frac{3}{3 - b^2}}, \quad r = (s_1 - s_2)/2, \quad (25)$$

and the orientation of \mathbf{n} with respect to the major principal stress axis is

$$\theta = 45^\circ - \psi/2. \quad (26)$$

The angle ψ of \mathbf{m} with respect to the discontinuity line may be determined by

$$\sin\psi = \sqrt{\frac{3b^2}{3 - b^2}}.\quad (27)$$

See Figure 2 for a visual description of θ and ψ .

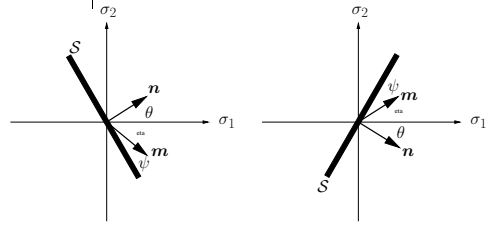


Figure 2. Slip line orientation with respect to major principal stress axis.

From Eq. (13), the stress-displacement relation governing the evolution of the jump displacement relative to the resolved stress is determined as

$$\dot{Q}_S := \dot{q} + \frac{\sqrt{3}\beta}{\sqrt{3 - b^2}}\dot{p} = \frac{\mathcal{H}_\delta}{3 - b^2}\dot{\zeta} \quad (28)$$

where $q = \mathbf{m} \cdot \mathbf{s} \cdot \mathbf{n}$, $\mathcal{H}_\delta = 3b^2K_\delta + H_\delta$, and \dot{Q}_S is the resolved stress rate along the discontinuity \mathcal{S} .

Note that by setting $\bar{\phi} = \bar{\psi} = 0$ the J2 flow (von Mises) plasticity model is recovered, which is useful for modeling the undrained condition in a cohesive soil.

With the constitutive model in place, the finite element implementation will proceed.

4 FINITE ELEMENT IMPLEMENTATION

The non-associated Drucker-Prager plasticity model with strong discontinuity is implemented within the framework of the assumed enhanced strain finite element method formulated by Simo & Rifai (1990), thus taking advantage of its convergence properties (i.e. stability and consistency). The discretized weak form of the equilibrium equations is expressed as (Simo & Oliver 1994)

$$\begin{aligned}\int_\Omega \nabla \bar{\boldsymbol{\eta}}^h : \boldsymbol{\sigma} \, d\Omega &= \int_\Omega \bar{\boldsymbol{\eta}}^h \cdot \mathbf{f} \, d\Omega + \int_\Gamma \bar{\boldsymbol{\eta}}^h \cdot \mathbf{t} \, d\Gamma \\ \int_{\Omega_{\text{loc}}^e} \tilde{\boldsymbol{\gamma}}^h : \boldsymbol{\sigma} \, d\Omega &= 0\end{aligned}\quad (29)$$

where $\bar{\boldsymbol{\eta}}^h$ is the continuous part of the discretized displacement variation in the space of admissible discretized test functions \mathcal{V}^h , \mathbf{f} and \mathbf{t} are the prescribed body and traction forces, respectively, e is in the set of localized elements, and $\tilde{\boldsymbol{\gamma}}^h \in \tilde{\mathcal{E}}^h$ is the enhanced strain variation in the space of admissible enhanced strain variations $\tilde{\mathcal{E}}^h$.

With the appropriate choice of standard and enhanced shape functions (see Figs 3 and 4 for details regarding the enhanced shape functions for a quadrilateral element), the following matrix governing equations result

$$\begin{aligned}
\mathbf{r}^e &:= \int_{\Omega^e} \mathbf{B}^t \boldsymbol{\sigma} d\Omega - \mathbf{f}_{\text{ext}}^e = \mathbf{0} \\
\mathbf{f}_{\text{ext}}^e &= \int_{\Omega^e} \mathbf{N}^t \mathbf{f} d\Omega - \int_{\partial_t \Omega^e} \mathbf{N}^t \mathbf{t} d\Gamma \\
b^e &:= (A^e)^{-1} \int_{\Omega_{\text{loc}}^e} \mathbf{F}^t \boldsymbol{\sigma} d\Omega - Q_S(t) = 0 \quad (30) \\
\mathbf{F} &= \left[\mathbf{m} \otimes \mathbf{n} + (\beta - b) \mathbf{1} / \sqrt{3(3 - b^2)} \right] \\
Q_S(t) &= Q_S(0) + \mathcal{H}_\delta \zeta^e / (3 - b^2)
\end{aligned}$$

where \mathbf{B} is the standard strain-displacement matrix, \mathbf{N} is the matrix of standard shape functions, A^e is the area of element e , \mathbf{F} and $\boldsymbol{\sigma}$ are in vector form, time $t = 0$ at onset of localization, and \mathbf{r}^e and b^e are the corresponding residuals for element e . Linearization of \mathbf{r}^e and b^e lends the matrix equations amenable to solution by the Newton-Raphson method (see Borja & Regueiro 1998 for details).

The numerical implementation of the localization condition in Eq. (25) is as follows:

$$\begin{aligned}
\text{IF} & \quad \left| \sqrt{\frac{3}{3 - b^2}} - \frac{\|\mathbf{s}_{n+1}\|}{\sqrt{2}r_{n+1}} \right| \leq h^{\text{tol}} \\
\text{THEN} & \quad \text{the element has localized} \quad (31)
\end{aligned}$$

where $h^{\text{tol}} = 1 \times 10^{-5}$ for the numerical simulations presented next.

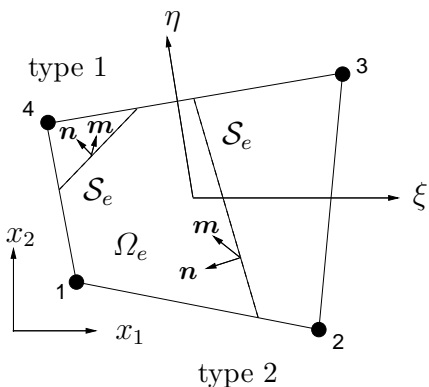


Figure 3. Two slip line types in a quadrilateral element.

5 NUMERICAL SIMULATION OF SHEAR BANDING IN GOSFORD SANDSTONE

The model is now used to attempt to simulate the behavior of a soft rock under plane strain compression loading while demonstrating mesh independent finite element solutions. The experimental setup and results for plane strain compression experiments on Gosford sandstone are delineated by

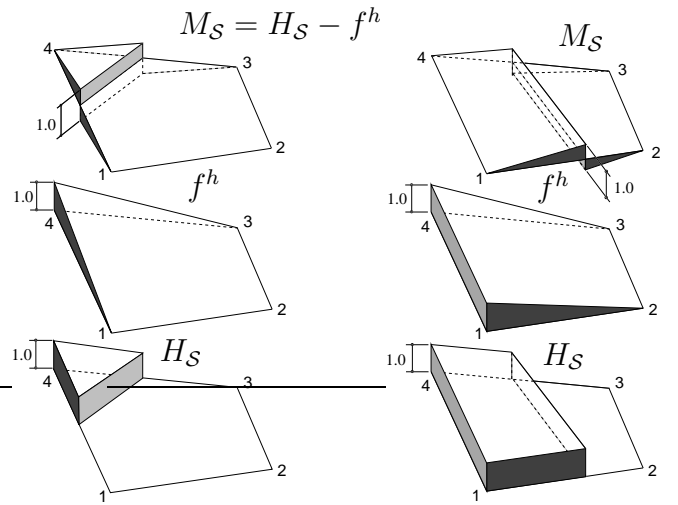


Figure 4. Slip line types 1 and 2. Enhanced shape functions M_S .

Ord et al. (1991). In particular, here we consider only the experiment labeled RAO640. A plane strain stress condition was achieved in the experimental setup by preventing deformation from occurring in the out-of-plane direction via a stiff, passive constraint. In addition, the lower platen was supported by steel rollers, thus allowing lateral movement of the sample and development of shear bands. Further details of the experimental setup can be found in Ord et al. (1991).

We found the value of modulus of elasticity E reported by Ord et al. (1991) to be low and inconsistent with the initial tangent modulus of the stress-strain curve for the specimen used in experiment RAO640, and thus we calculated E directly from the reported stress-strain curve assuming homogeneous, linear elastic, plane strain behavior up until the yield point:

$$\frac{\Delta(\sigma_{22} - \sigma_{11})}{\Delta \epsilon_{22}} = \frac{2\mu}{1 - \nu} \quad (32)$$

where $\Delta(\cdot)$ implies increment of a quantity, $\mu = E/(2(1 + \nu))$, 2 is the direction of compressive loading, and 1 is the direction of confining pressure. Using the reported value for Poisson's ratio $\nu = 0.31$ in Eq. (32), we found $E = 15.3$ GPa. The remaining reported parameters include cohesion $\bar{c} = 8$ MPa, friction angle $\bar{\phi} = 44^\circ$, average dilation angle $\bar{\psi} = 20^\circ$, and confining pressure $\sigma_1 = 15$ MPa. The standard hardening/softening moduli are chosen to best represent the experimental deviatoric load-displacement curve up until the peak stress level ($H' = -1$ GPa, $K' = 0$), while the localized hardening/softening moduli are chosen to best represent the slope of the experimental deviatoric load-displacement curve after failure surface

formation at peak stress level ($H_\delta = -50, -55$ GPa/m, $K_\delta = 0$; written per meter because the Dirac-delta function has an implicit dimension of 1/length). The second value of H_δ corresponds to that used for the simulation in which $\bar{\psi} = 15^\circ$. The dilation angle $\bar{\psi} = 15^\circ$ is considered to understand what effect a dilation angle lower than the reported average dilation angle would have on the simulation results. In addition, a post-localization dilation angle, $\bar{\psi}_{loc} = 5^\circ$, is chosen to represent the near negligible dilation exhibited once localized deformation begins to develop.

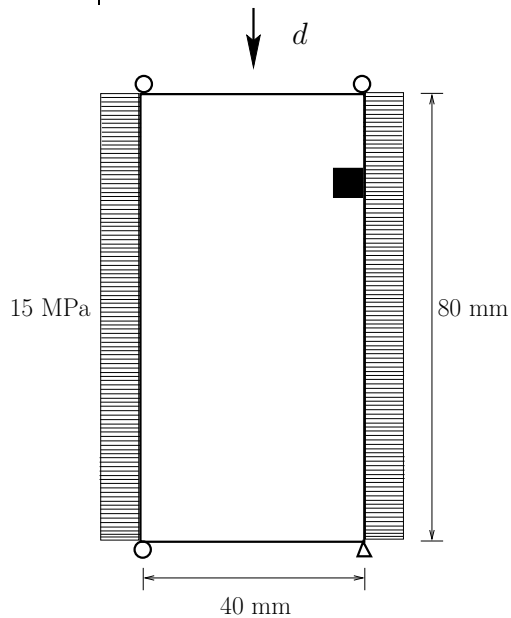


Figure 5. Finite element model boundary conditions for plane strain compression of Gosford sandstone. Confining pressure is 15 MPa. Prescribed displacement d . Location of weakened element shaded black.

The sample measures $40 \times 80 \times 80$ mm (80 mm being the height of the sample and also the out-of-plane thickness, with 40 mm as the width) and is discretized by 128 and 512 linear quadrilateral elements in order to demonstrate objectivity with respect to mesh refinement. Frictionless boundaries are assumed (see Fig. 5), and the top boundary is displaced downward at given increments, while measuring the reaction forces at the bottom boundary to be able to plot load-displacement curves. The cohesion of one side element of each mesh is lowered by 1% to perturb the uniform stress state and to clearly define where the slip line initiates; see Figure 5 for location. Another approach would be to include friction at the loading platens via contact elements to simulate an inhomogeneity in the loading which would trigger a non-uniform stress state.

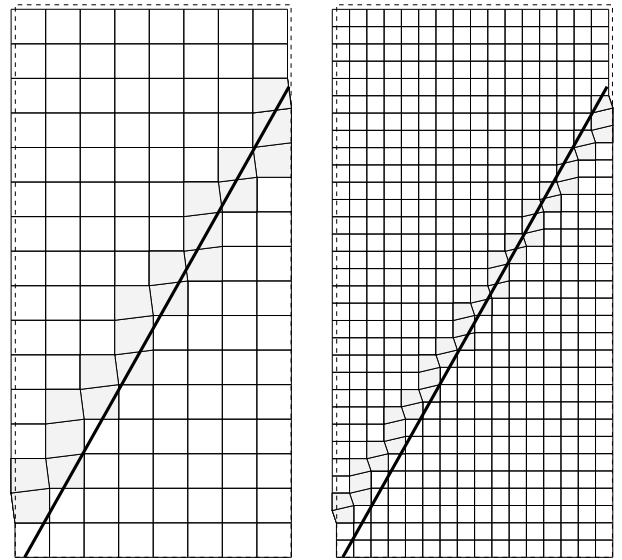


Figure 6. Deformed meshes for enhanced finite element solutions with 128 and 512 linear quadrilateral elements ($\bar{\psi} = 20^\circ$). Localized elements are shaded. Insensitivity to mesh alignment demonstrated by the slip line tracing across element sides. Actual failure surface orientation drawn as a solid line on the meshes.

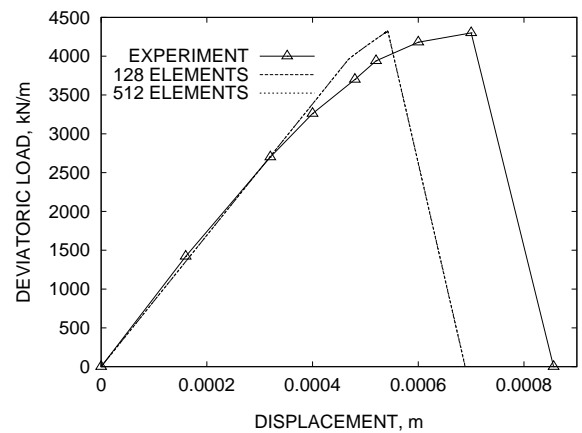


Figure 7. Enhanced finite element solutions with 128 and 512 linear quadrilateral elements ($\bar{\psi} = 20^\circ$, $A = 0.15$ for Eq. (23)). Curves are one on top of the other, demonstrating objectivity with respect to mesh refinement.

Deformed meshes are shown in Figures 6 and 8, with corresponding deviatoric load-displacement curves shown in Figures 7 and 9. Mesh independence is observed as the slip line propagates across elements without having the element sides aligned with the expected slip line orientation (elements through which the slip line has propagated are shaded gray), and by the deviatoric load-displacement curves lying one on top of the other.

The linear elastic portion of the load-displacement curves proceeds up until yield-

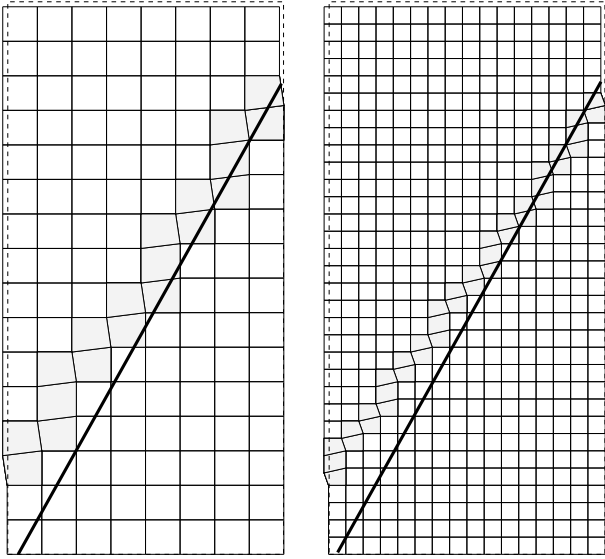


Figure 8. Deformed meshes for enhanced finite element solutions with 128 and 512 linear quadrilateral elements ($\bar{\psi} = 15^\circ$). Localized elements are shaded. Insensitivity to mesh alignment demonstrated by the slip line tracing across element sides. Actual failure surface orientation drawn as a solid line on the meshes.

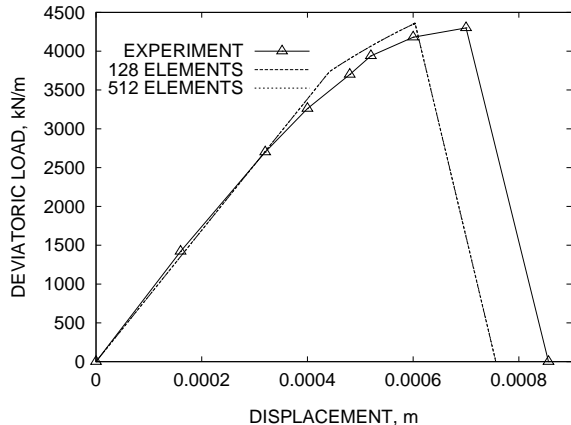


Figure 9. Enhanced finite element solutions with 128 and 512 linear quadrilateral elements ($\bar{\psi} = 15^\circ$, $A = 0.25$ for Eq. (23)). Curves are one on top of the other, demonstrating objectivity with respect to mesh refinement.

ing, a plastic region follows up until peak load at which time localization is detected, and then the slip line propagates through the mesh at peak load resulting in subsequent linear softening along the discontinuity (i.e. the slip line). Note that the slip line would propagate through the mesh over a wider range of displacement prior to peak load if the stress state was more non-uniform (see excavation simulations in Borja & Regueiro 1998). In this plane strain compression simulation, more inhomogeneities throughout the mesh (i.e. per-

turbed elements with cohesion values lower than the reported value of $\bar{c} = 8$ MPa) would produce a more non-uniform stress state.

The $\bar{\psi} = 15^\circ$ case shows more of a plastic region than the $\bar{\psi} = 20^\circ$ case does, but does not represent the failure surface orientation as well. The failure surface measures $\approx 30^\circ$ from the major compressive principal stress axis for the actual sample (see Fig. 9c of Ord et al. (1991)) and is represented by solid lines drawn on the meshes in Figures 6 and 8. Meshes in Figure 6 predict a failure surface orientation of 35° with respect to the major compressive principal stress axis, and meshes in Figure 8 predict 37.5° .

6 SUMMARY AND FUTURE WORK

A non-associated Drucker-Prager plasticity model was formulated in the context of strong discontinuities and implemented within the framework of the assumed enhanced strain finite element method. A numerical simulation of shear banding in Gosford sandstone was conducted in a mesh-independent manner. The numerical results show promise for the use of the model as a predictive computational tool.

Ongoing work includes extending the model for three dimensional analysis, which would allow simulation of shear banding in triaxial compression experiments, and incorporating the fluid phase and nonlinear geometric effects to be able to model the behavior of realistic, in situ geomechanical structures which are susceptible to developing localized deformation.

7 ACKNOWLEDGEMENT

The work presented in this paper was supported by the G3S Division of the National Science Foundation through Grant No. CMS97-00426 under the directorship of Dr. Priscilla P. Nelson. This support is gratefully acknowledged.

REFERENCES

- Adachi, T., F. Oka, & A. Yashima 1991. A finite element analysis of strain localization for soft rock using a constitutive equation with strain softening. *Arch. Appl. Mech.* 61:183–191.
- Armero, F. & K. Garikipati 1995. Recent advances in the analysis and numerical simulation of strain localization in inelastic solids. In D.R.J. Owen,

- E. Oñate, & E. Hinton (eds), CIMNE, *Proceedings of Computational Plasticity IV, Barcelona, Spain, April 1995*: 547–561.
- Armero, F. & K. Garikipati 1996. An analysis of strong-discontinuities in multiplicative finite strain plasticity and their relation with the numerical simulation of strain localization in solids. *Int. J. Solids Structures*. 33:2863–2885.
- Bažant, Z.P., & G. Pijaudier-Cabot 1988. Nonlocal continuum damage, localization instability and convergence. *J. Appl. Mech.*, 55:287–293.
- Borja, R.I., & R.A. Regueiro 1998. Strain localization in frictional materials exhibiting displacement jumps. *Comp. Meth. Appl. Mech. Eng.*, in review.
- Garikipati, K., & T.J.R. Hughes 1998. A study of strain localization in a multiple scale framework—the one dimensional problem. *Comp. Meth. Appl. Mech. Eng.*, to appear.
- Hill, R. 1962. Acceleration waves in solids. *J. Mech. Phys. Solids*. 10:1–16.
- Kachanov, L.M. 1971. *Foundations of the Theory of Plasticity*. Amsterdam: North-Holland.
- Labuz, J.F., S.-T. Dai, & E. Papamichos 1996. Plane-strain compression of rock-like materials. *Int. J. Rock Mech. Min. Sci. & Geomech. Abstr.* 33:573–584.
- Larson, R., & K. Runesson 1993. Discontinuous displacement approximation for capturing plastic localization. *Int. J. Num. Meth. Eng.*, 36:2087–2105.
- Lubliner, J. 1990. *Plasticity Theory*. New York: Macmillan.
- Matthies, H., G. Strang, & E. Christiansen 1979. The saddle point of a differential program. In R. Glowinski, E.Y. Rodin, & O.C. Zienkiewicz (eds), *Energy Methods in Finite Element Analysis*. New York: Wiley.
- Ord, A., I. Vardoulakis, & R. Kajewski 1991. Shear band formation in Gosford sandstone. *Int. J. Rock Mech. Min. Sci. & Geomech. Abstr.* 28:397–409.
- Ortiz, M., Y. Leroy, & A. Needleman 1987. A finite element method for localized failure analysis. *Comput. Methods Applied Mech. Engrg.*, 61:189–214.
- Owen, D.R.J., & E. Hinton 1980. *Finite Elements in Plasticity: Theory and Practice*. Swansea: Pineridge.
- Pietruszczak, S.T., & Z. Mróz 1981. Finite element analysis of deformation of strain-softening materials. *Int. J. Num. Meth. Eng.* 17:327–334.
- Rice, J.R. The localization of plastic deformation. In W.T. Koiter (ed), *Theoretical and Applied Mechanics*. 207–220. North-Holland. 17:327–334.
- Santarelli, F.J., & E.T. Brown 1989. Failure of three sedimentary rocks in triaxial and hollow cylinder compression tests. *Int. J. Rock Mech. Min. Sci. & Geomech. Abstr.* 26:401–413.
- Simo, J.C. 1996. Topics on the numerical analysis and simulation of plasticity. In P.G. Ciarlet & J.L. Lions (eds), *Handbook of Numerical Analysis*. Vol. III. New York: Elsevier.
- Simo, J.C., J. Oliver, & F. Armero 1993. An analysis of strong discontinuities induced by strain-softening in rate-independent inelastic solids. *Computational Mechanics*. 12:277–296.
- Simo, J.C., & J. Oliver 1994. A new approach to the analysis and simulation of strain softening in solids. In Z.P. Bažant, Z. Bittnar, M. Jirasek, & J. Mazars (eds), *Fracture and Damage in Quasibrittle Structures*. 25–39. New York: E & FN Spon.
- Simo, J.C., & M.S. Rifai 1990. A class of mixed assumed strain methods and the method of incompatible modes. *Int. J. Num. Methods in Engrg.* 29:1595–1638.
- Stakgold, I. 1979. *Green's Functions and Boundary Value Problems*. New York: Wiley.
- Vardoulakis, I., & M. Goldschieder 1981. Biaxial apparatus for testing shear bands in soils. *Soil Mechanics and Foundation Engineering: Tenth International Conference*. 1:819–824.
- Wan, R.G., D.H. Chan, & N.R. Morgenstern 1990. A finite element method for the analysis of shear bands in geomaterials. *Finite Elem. Anal. Des.* 7:129–143.
- Wawersik, W.R., J.W. Rudnicki, W.A. Olsson, D.J. Holcomb, & K.T. Chau 1990. Localization of deformation in brittle rock: theoretical and laboratory investigations. In S.P. Shah, S.E. Swartz, & M.L. Wang (eds), *Micromechanics of Failure of Quasi-Brittle Materials*. 115–124. New York: Elsevier.
- Yumlu, M., & M.U. Ozbay 1995. A study of the behaviour of brittle rocks under plane strain and triaxial loading conditions. *Int. J. Rock Mech. Min. Sci. & Geomech. Abstr.* 32:725–733.
- Zienkiewicz, O.C., M. Pastor, & M. Huang 1995. Softening, localisation and adaptive remeshing. Capture of discontinuous solutions. *Computational Mechanics* 17:98–106.